

The influence of Sn doping on the growth of In_2O_3 on Y-stabilized $\text{ZrO}_2(100)$ by oxygen plasma assisted molecular beam epitaxy

A. Bourlange,¹ D. J. Payne,¹ R. G. Palgrave,¹ H. Zhang,¹ J. S. Foord,¹ R. G. Egddell,^{1,a)} R. M. J. Jacobs,¹ T. D. Veal,² P. D. C. King,² and C. F. McConville²

¹*Department of Chemistry, Chemistry Research Laboratory, Mansfield Road, Oxford OX1 3TA, United Kingdom*

²*Department of Physics, University of Warwick, Coventry CV4 7AL, United Kingdom*

(Received 24 March 2009; accepted 19 May 2009; published online 1 July 2009)

The influence of Sn doping on the growth of In_2O_3 on Y-stabilized $\text{ZrO}_2(100)$ by oxygen plasma assisted molecular beam epitaxy has been investigated over a range of substrate temperatures between 650 and 900 °C. The extent of dopant incorporation under a constant Sn flux decreases monotonically with increasing substrate temperature, although the n -type carrier concentration in “overdoped” films grown at 650 °C is lower than in films with a lower Sn concentration grown at 750 °C. The small increase in lattice parameter associated with Sn doping leads to improved matching with the substrate and suppresses breakup of the films into square islands observed in high temperature growth of undoped In_2O_3 on Y-stabilized $\text{ZrO}_2(100)$. Plasmon energies derived from infrared reflection spectra of Sn-doped films are found to be close to satellite energies in core level photoemission spectroscopy, but for a nominally undoped reference sample there is evidence for carrier accumulation at the surface. This influences both the In $3d$ core line shape and the intensity of a peak close to the Fermi energy associated with photoemission from the conduction band.

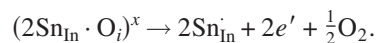
© 2009 American Institute of Physics. [DOI: 10.1063/1.3153966]

I. INTRODUCTION

Indium oxide (In_2O_3) is a wide gap material that adopts the bixbyite structure. The unit cell is body centered cubic and belongs to the space group $Ia3$ (Ref. 1). It is derived from a $2 \times 2 \times 2$ superstructure of fluorite but with $\frac{1}{4}$ of the anion sites vacant. There are 16 formula units per cell and the lattice parameter a is usually quoted to be 10.117 Å. However In_2O_3 can tolerate significant concentrations of oxygen vacancies to give $\text{In}_2\text{O}_{3-\delta}$ and the lattice parameter is dependent on the degree of nonstoichiometry. The vacancies act as n -type donors.² In_2O_3 is also amenable to degenerate n -type doping by substitution of Sn cations onto In sites to give so-called indium tin oxide (ITO).^{3–6} ITO is one of a very restricted range of materials that combines the properties of optical transparency in the visible region with a high electrical conductivity. The increasing cost of indium means that ITO films are now much more expensive to produce than degenerately doped SnO_2 films (the cost of raw In has been as high as \$250/kg recently, as compared with around \$13/kg for Sn). However due to the higher electron mobility, ITO remains the material of choice as a transparent conducting electrode in solar cells, liquid crystal displays, and electroluminescent display devices.

The solubility limit of Sn in bulk ceramic samples of In_2O_3 prepared by conventional solid state synthesis is around 6%, corresponding to a dopant atom concentration of 1.85×10^{21} atoms cm^{-3} (Refs. 7 and 8). Higher doping levels are attained in ITO thin films, which typically incorporate around 10 cation % of Sn (3.08×10^{21} atoms cm^{-3}) in com-

mercially available films, although even higher levels of Sn incorporation beyond even 20% are possible with retention of the bixbyite phase.^{9,10} However the highest carrier concentration n that can be achieved in ITO thin films is typically around 1.5×10^{21} cm^{-3} , and both n and the conductivity decrease for Sn doping levels above about 10% (Refs. 9 and 10). The difference between the Sn concentration and the free carrier concentration is attributed to compensation of Sn doping by incorporation of oxygen into interstitial positions within the relatively open bixbyite structure. The interstitials form so-called Köstlin clusters^{9,10} by association with two substitutional Sn ions to give $(2\text{Sn}_{\text{In}} \cdot \text{O}_i)^x$ in Kröger–Vink notation. The Köstlin cluster is electrically neutral but can give rise to two n -type charge carriers under conditions of low oxygen partial pressure:



At the highest Sn doping levels there is evidence^{10–13} for further aggregation of Sn ions and interstitials to give so called nonreducible clusters. The six-coordinate ionic radius of Sn^{4+} in the Shannon and Prewitt tabulation¹⁴ has a value of 0.83 Å, which is 0.11 Å smaller than the value of 0.94 Å for In^{3+} . However, Sn doping in In_2O_3 leads to an increase in the lattice parameter.^{7,10,15} This appears to be due to population of conduction band states which are In–O antibonding: the increase in lattice parameter with Sn doping is more pronounced for thin films prepared under reducing conditions than for films prepared under the oxidizing conditions that lead to pronounced compensation of the n -type donors and therefore lower occupation of the conduction band.¹⁰

Despite the enormous technological importance of ITO,^{3–6} very little effort has been directed toward growth of

^{a)}Author to whom correspondence should be addressed. Electronic mail: russell.egddell@chem.ox.ac.uk.

high quality thin films of In_2O_3 or ITO. To date most work on growth of epitaxial single crystal In_2O_3 films has concentrated on deposition of In_2O_3 on alumina and yttria-stabilized zirconia single crystal substrates by pulsed laser deposition in ultrahigh vacuum compatible chambers,^{16–19} although there are some reports of single crystal growth by metal organic chemical vapor deposition²⁰ and by molecular beam epitaxy (MBE) using conventional indium Knudsen cells and oxygen atom plasma sources.^{21–23} These considerations have prompted us to initiate a program concerned with growth of In_2O_3 and ITO thin films on cubic zirconia by oxygen plasma assisted MBE. Improvements in the conductivity of ITO could lead to use of thinner films in the various technologies discussed above, which would in turn have a significant economic impact given the high cost of In. ZrO_2 itself has a low symmetry monoclinic structure at room temperature, but a cubic phase can be stabilized by replacement of some of the Zr^{4+} with the larger cation Y^{3+} , with concomitant introduction of compensating oxygen vacancies. The face centered cubic fluorite structure of Y-stabilized ZrO_2 belongs to the space group $Fm\bar{3}m$. For the minimum Y concentration of around 17% required to stabilize the cubic phase the lattice parameter can be estimated as $a=5.142 \text{ \AA}$ (Refs. 24–26). Thus at 17% Y-doping there is a mismatch of 1.6% between $2a$ for Y– ZrO_2 and a for In_2O_3 . Moreover the two structures involve basically similar cation arrays but with $\frac{1}{4}$ of the anion sites of the fluorite structure vacant in In_2O_3 so that the cations are six-coordinate rather than eight-coordinate as in fluorite. Thus Y-doped ZrO_2 appears to be an ideal substrate for growth of well-ordered thin films of In_2O_3 . Our work to date has shown that growth of In_2O_3 on Y– ZrO_2 at temperatures around 650 °C by MBE leads to continuous epitaxial films,²⁷ but growth at high temperatures leads to breakup of the films into micron sized square islands, which allows some relief of the strain due to lattice mismatch.^{28,29} Analysis of the position of the valence band onset relative to the Fermi energy in high quality x-ray photoemission spectra of continuous epitaxial films³⁰ has led to the realization that the bandgap of In_2O_3 must be much less than the widely quoted value of 3.75 eV (Refs. 31–33) and that there is pronounced surface electron accumulation for low bulk doping levels due to surface states which pin the Fermi level above the conduction band minimum.³⁴

In the present communication we explore the influence of Sn doping on the growth of In_2O_3 on Y-stabilized $\text{ZrO}_2(100)$ substrates. The main parameter that has been varied is the substrate temperature. It emerges that the extent of Sn incorporation is strongly temperature dependent, leading to an increase in lattice parameter as compared with undoped films that is bigger at low temperature than at high temperature. Sn doping acts to reduce the mismatch between the lattice parameters of the substrate and the epilayer. This, in turn, has a striking influence on film morphology and leads to enhanced electron mobility in optimally Sn-doped films.

II. EXPERIMENTAL PROCEDURE

Undoped and Sn-doped In_2O_3 films were grown on $1 \times 1 \text{ cm}^2$ Y-stabilized $\text{ZrO}_2(100)$ substrates with a nominal Y

doping level of 17% (as defined by the formula $\text{Zr}_{1-x}\text{Y}_x\text{O}_{2-x/2}$ with $x=0.17$) in an ultrahigh vacuum oxide MBE system (SVT, USA) with a base pressure of 5×10^{-8} Pa. This incorporated liquid nitrogen cooled cryopanel, a hot-lip indium Knudsen cell and a conventional Sn Knudsen cell. Oxygen atoms were generated in a radio frequency (rf) plasma source operated at 200 mW rf power with an oxygen background pressure of 2×10^{-3} Pa. Substrates were held by gravity in a recessed Mo mounting plate and heated radiatively using a graphite filament. The substrate temperature was measured by a chromel-alumel thermocouple spot welded to the cradle holding the sample mounting plate. Substrates were cleaned by exposure to the oxygen atom beam with a measured substrate temperature of 900 °C. Films were then grown over a range of substrate temperatures between 650 and 900 °C in growth runs whose duration extended over a time of $3 \times 10^3 \text{ s}$ (50 min). The In cell was operated at a temperature of 780 °C which gave a deposition rate of 0.01 nm s^{-1} for In metal in the absence of an O flux as monitored by a quartz crystal monitor offset from the substrate position. The true growth rate of In_2O_3 on the substrate was found to be about 0.04 nm s^{-1} . The Sn cell was operated a fixed temperature of 840 °C. This gave a deposition rate for Sn metal on the monitor (0.008 nm s^{-1}) just below that for In metal, but as to be discussed below the extent of Sn incorporation into the doped oxide films was very much lower than that of In and is very strongly substrate temperature dependent.

Surface order in the as-grown films was monitored by low energy electron diffraction carried out *in situ* in an analysis chamber adjacent to the MBE growth chamber. Other characterization was carried out *ex situ*. Atomic force microscopy (AFM) images were recorded in a Digital Instruments multimode scanning probe microscopy instrument with a Nanoscope IIIa controller. This was usually operated in tapping mode but images of samples grown at 650 °C were recorded in contact mode. The measurements employed a “J” scanner having a lateral range of approximately 100 μm and a vertical range of 6 μm . Silicon probes (Nascatec GmbH model NST NCHFR), with resonant frequencies of approximately 320 kHz were used. X, Y, and Z calibration of the AFM was accomplished by scanning a 10 μm pitch 200 nm three-dimensional reference from Digital Instruments.

High-resolution x-ray photoelectron spectra (XPS) were measured at 45° off take angle in a Scienta ESCA 300 spectrometer. This incorporates a rotating anode $\text{Al K}\alpha$ ($h\nu = 1486.6 \text{ eV}$) x-ray source, a seven crystal x-ray monochromator and a 300 mm mean radius spherical sector electron energy analyzer with parallel electron detection system. The x-ray source was run with 200 mA emission current and 14 kV anode bias, while the analyzer operated at 150 eV pass energy with 0.8 mm slits. Gaussian convolution of the analyzer resolution with a linewidth of 260 meV for the x-ray source gives an effective instrument resolution of 400 meV. Due to the highly insulating nature of the substrate, sample charging was problematic and it was necessary to stabilize the surface charge with an electron flood gun delivering low

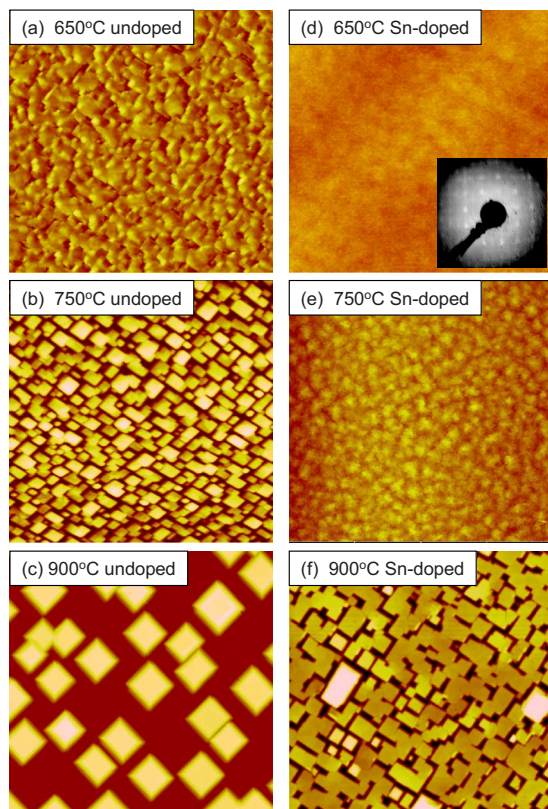


FIG. 1. (Color online) $10 \times 10 \mu\text{m}^2$ images of undoped [(a)–(c)] and Sn-doped [(d)–(f)] In_2O_3 grown on Y-stabilized $\text{ZrO}_2(100)$ at the temperatures indicated under constant In [(a)–(c)] or In+Sn [(d)–(f)] fluxes. The z -range in the images extend over the following ranges (a) 126 nm, (b) 150 nm, (c) 500 nm, (d) 2 nm, (e) 10 nm, and (f) 200 nm. The inset in panel (d) shows the LEED pattern from the as-grown film measured *in situ* in the MBE UHV system.

energy electrons. Binding energies were referenced to the Fermi edge associated with occupied conduction band states that was observed for all samples.

θ - 2θ x-ray diffraction scans were performed on a Philips Xpert diffractometer using monochromatic $\text{Cu } K\alpha$ radiation ($\lambda = 1.54060 \text{ \AA}$). Single-field (0.55 T) Hall effect measurements were performed on the samples in the Van der Pauw geometry at room temperature. IR reflectivity measurements were performed on a Perkin-Elmer Spectrum GX Fourier transform infrared spectrometer, with a 35° specular reflection to the surface normal. A high-reflectivity optical mirror was used as a reference.

III. RESULTS AND DISCUSSION

A. Morphology and extent of Sn incorporation

$10 \times 10 \mu\text{m}^2$ AFM images of undoped In_2O_3 films grown at substrate temperatures of 650, 750, and 900 °C are shown in panels (a)–(c) of Fig. 1. As reported previously films grown at 650 °C are continuous^{27,29} but with evidence of development square columns or islands, with edges oriented along $\langle 110 \rangle$ directions of the substrate. The films are quite rough with a z scale extending over a range of 150 nm for the image in Fig. 1(a). The film grown at 900 °C has a completely different morphology and is made up of an array of isolated square islands with typical edge sizes of $1 \mu\text{m}$

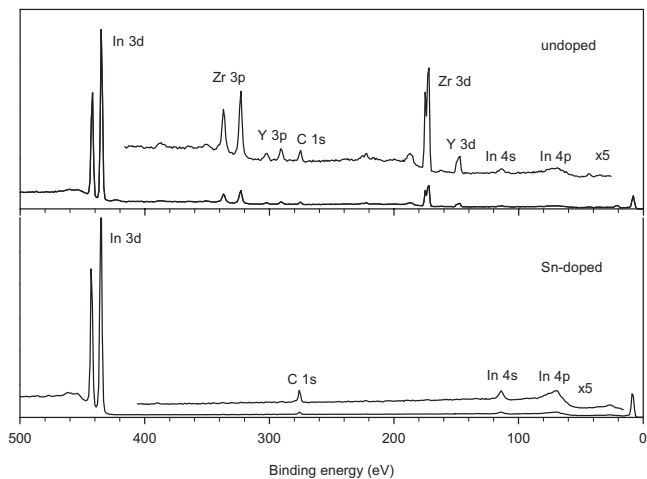


FIG. 2. XPS of undoped In_2O_3 and Sn-doped In_2O_3 grown at 900 °C across the range encompassing the In 3d and Zr and Y 3p and 3d core lines.

and thicknesses of 500 nm, again oriented parallel to $\langle 110 \rangle$ directions of the substrate.^{28,29} The film grown at 750 °C has an intermediate morphology, with more clearly defined island or columnar structure than at 650 °C, but with some remaining connectivity between the islands.

Sn doping under a constant Sn flux leads to dramatic changes in film morphology as shown in panels (d)–(f) of Fig. 1. The doped film deposited at 650 °C substrate temperature is very much smoother than the undoped film and the virtually featureless AFM image of Fig. 1(d) has a dramatically reduced z range of 2 nm, with a root mean square (rms) roughness of only 0.25 nm. The smooth morphology on the micron length range is accompanied by good short range atomic order which allows observation of well defined square LEED patterns, as expected for the (100) surface of a cubic material. The doped film deposited at 750 °C is also smooth (z range 10 nm with an rms roughness of 1 nm) and continuous. There is no indication of the incipient island formation observed for the undoped film. The doped film grown at 900 °C shows an interesting and distinct morphology. The surface is mostly quite smooth but with a number of deep trenches running along the $\langle 110 \rangle$ directions. However, in contrast to the undoped film, there remains some connectivity between the islandlike blocks. Moreover it was found that strong Zr and Y 3p and 3d core level substrate peaks observed in XPS of the undoped film grown at 900 °C were completely suppressed by Sn doping at the same growth temperature (Fig. 2), implying complete coverage of the substrate even in the region of the deep trenches observed in Fig. 1(f).

The extent of Sn incorporation into the doped films was studied by measurement of the In 3d and Sn 3d core lines (Fig. 3). The film grown at 650 °C displays very intense Sn 3d core lines. After correction for atomic sensitivity factors³⁵ we may infer a surface Sn doping level $2x \times 100\%$ defined by the formula $\text{In}_{2-x}\text{Sn}_x\text{O}_{3\pm y}$ equal to 16.6%. This sample is strongly “overdoped” as compared to conventional ITO which typically has around 10% Sn doping. The surface doping level drops to 7.5% for the sample grown at 750 °C substrate temperature and to only 0.66%

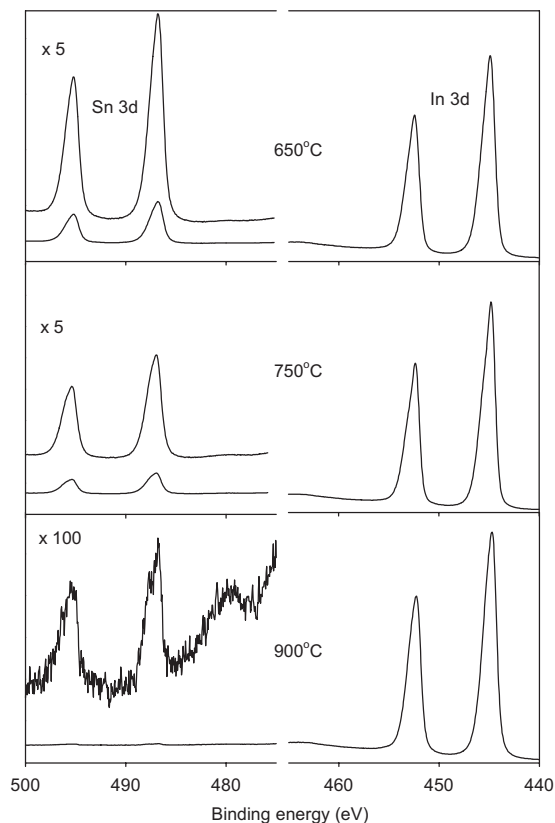


FIG. 3. XPS of Sn-doped In_2O_3 grown at the temperatures indicated across the In 3d and Sn 3d core lines.

for the sample grown at 900 °C. Since we operated under a constant Sn flux, we must conclude that the accommodation of the Sn dopant into the growing film decreases dramatically with increasing temperature. This conclusion parallels observations that have been made on the MBE growth of SnO_2 on $\text{TiO}_2(110)$.³⁶ Here it appears that the sticking probability for Sn under an O flux identical to that used in the current growth runs decreases dramatically for substrate temperatures above 775 °C. A marked decrease in SnO_2 growth rate in plasma MBE with increasing substrate temperature was also found by Tsai *et al.*³⁷ This contrasts with the behavior of In where the growth rate for In_2O_3 seems largely independent of temperature between 650 and 900 °C. The striking difference is probably attributable to the fact that Sn forms a stable lower oxide—SnO—in an oxidation state that is two lower than the group oxidation state. SnO is much more volatile than SnO_2 and the volatility of SnO has been exploited in crystal growth by vapor transport of SnO_2 under reducing conditions.³⁸ Despite the fact that Sn and In are adjacent to each other in Periodic Table there is no analogous stable lower oxide of In (i.e., In_2O is not known as a stable phase).

B. X-ray diffraction

θ -2 θ x-ray diffraction scans are shown in Fig. 4. The wide scan trace from the Sn-doped sample grown at 650 °C shown in Fig. 4(a) contains the (400) and (800) reflections of cubic In_2O_3 close, respectively, to the (200) and (400) reflections of the substrate, along with a very weak $\text{In}_2\text{O}_3(600)$

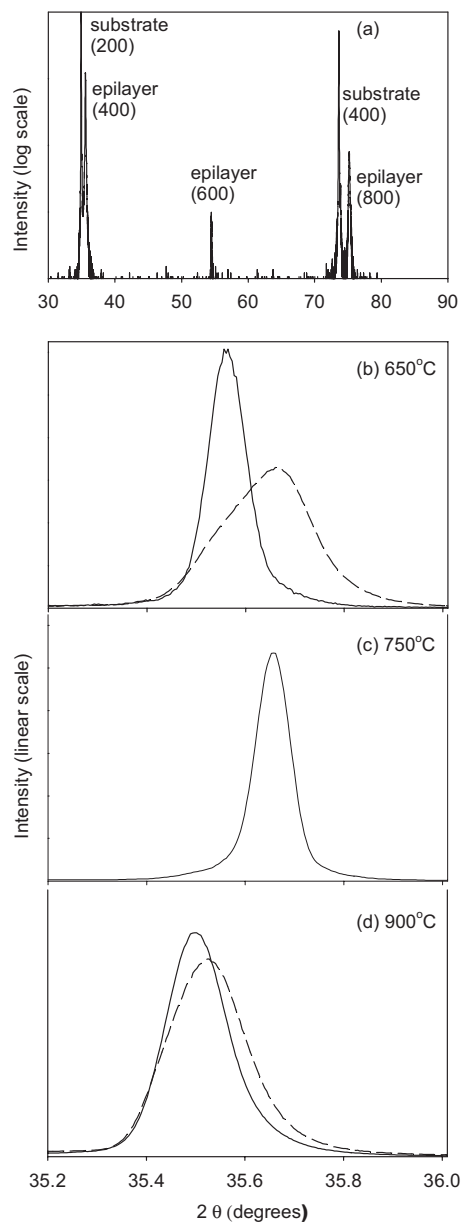


FIG. 4. θ -2 θ X-ray diffraction traces. (a) Wide scan trace including substrate (200) and (400) peaks and epilayer (400), (600), and (800) peaks for Sn-doped film grown at 650 °C. [(b)–(d)] Expanded views of epilayer (400) peaks for Sn-doped (solid line) and undoped (dashed line) In_2O_3 grown at the temperatures indicated.

reflection. The XRD demonstrates excellent phase purity in the epilayer despite the high Sn doping level as well as near perfect (100) orientation in the epilayer. Similar results were obtained from the other samples. Expansions of the (400) reflections from the epilayers are shown in the remaining panels while lattice parameters derived from these traces are given in Table I. The mean value for twice the cubic lattice parameter of the Y–ZrO₂ substrate is 10.276 ± 0.005 Å, which is slightly less than the value of 10.284 Å obtained by extrapolation of database values for lattice parameters for zirconias with a higher Y doping level. The apparent lattice parameter for undoped In_2O_3 increased from 10.060 Å for the film grown at 650 °C to 10.099 Å for the film grown at 900 °C. This increase has been explained on the basis that the continuous film grown at 650 °C is under lateral tension

TABLE I. Lattice parameters from analysis of XRD data.

Growth run		Y-ZrO ₂	In ₂ O ₃
		2a (Å)	a (Å)
650 °C	Undoped	10.271	10.060
	Sn-doped	10.272	10.091
750 °C	Sn-doped
	Sn-doped	10.283	10.064
900 °C	Undoped	10.276	10.099
	Sn-doped	10.277	10.107

due to mismatch with the substrate and must be significantly strained, which will lead to a decrease in the d spacing normal to the surface. This strain is relieved when the films break up into islands during high temperature growth.³⁹ However, an increase in lattice parameter could also be explained in terms of an increase in carrier concentration with increasing growth temperature. The (400) diffraction peak from the doped film grown at 650 °C is much narrower than for the undoped film and occurs at a lower diffraction angle, corresponding to an a value of 10.091 Å. This is consistent with the increase in lattice parameter produced by Sn doping in bulk samples.^{7,10,15} The increase in lattice parameter due to Sn doping leads to better lateral matching with the substrate, decreased tensile stress in the films and a smoother film morphology. Sn doping during growth at 900 °C leads to a much smaller increase in lattice parameter as compared to growth at 650 °C. Moreover the influence on the film morphology is less pronounced than for the films grown at 650 °C and a dissected, “limestone pavement” structure is observed even for the doped film. These observations are both consistent with the lower level of Sn incorporation at high substrate temperature. The doped film grown at 750 °C gives the narrowest (400) diffraction peak with a full width at half maximum (FWHM) of 0.09°. This peak width is of the order expected for a coherent single crystal film with thickness of the order of 100 nm. Somewhat surprisingly the measured lattice parameter (10.064 Å) is lower than for films grown at both 650 and 900 °C. It should be mentioned finally that although the changes in film morphology with Sn doping can be understood, in part, in terms of changes in lattice parameter associated with Sn doping, the Sn dopant may also have a pronounced effect on surface and interface energies which will further influence film structure. However it is not possible to quantify these effects at present.

C. Transport and electronic structure

Carrier concentrations in the films were studied by both single field Hall effect measurements and infrared reflectance spectroscopy, which probes the plasmon energy associated with the n -type charge carriers. The results of Hall measurements on the three continuous films (corresponding to panels (a), (d), and (e) of Fig. 1) are summarized in Table II. The sheet carrier concentrations were converted into bulk carrier concentrations assuming a layer thickness of 120 nm, in accordance with TEM observations on lamellar slices cut from the MBE-grown samples. The nominally undoped sample

TABLE II. Sheet electron density (N_s), mobility (μ) and volume electron density (n) from Hall measurements.

Sample	N_s (cm ⁻²)	μ (cm ² V ⁻¹ s ⁻¹)	n (cm ⁻³)
Undoped 650 °C	9.0×10^{13}	31.5	7.5×10^{18}
Sn-doped 650 °C	5.0×10^{15}	27.2	4.2×10^{20}
Sn-doped 750 °C	8.1×10^{15}	59.9	6.7×10^{20}

has a very low bulk carrier concentration of 7.5×10^{18} cm⁻³. The mobility has a relatively low value of only 31.5 cm² V⁻¹ s⁻¹, which is no greater than typical values for polycrystalline films.^{40,41} The low mobility is, however, not surprising given the obvious columnar structure of Fig. 1(a) and the corresponding large number of grain boundary interfaces. The carrier concentration for the Sn-doped film grown at 650 °C has a very much larger value of 4.2×10^{20} cm⁻³. Despite the pronounced improvement in the morphology of the film as gauged by AFM, the mobility remains low with a value again just below 30 cm² V⁻¹ s⁻¹. Here we must assume that there is very pronounced impurity scattering associated with the large concentration of Sn and the associated compensating oxygen interstitials in the K₂O clusters (see below). Despite the lower level of Sn incorporation, the sample grown at 750 °C has a higher carrier concentration of 6.7×10^{20} cm⁻³. Moreover the mobility is roughly twice that of the other samples with a value just below 60 cm² V⁻¹ s⁻¹. The lower carrier concentration in over-doped samples with Sn doping levels above 10% is in agreement with previous work discussed above.^{9,10}

The experimental infrared reflection spectra for the three continuous films are shown in Fig. 5. Simulations of the spectra were performed using a two-oscillator dielectric theory model⁴² to account for lattice and free carrier contri-

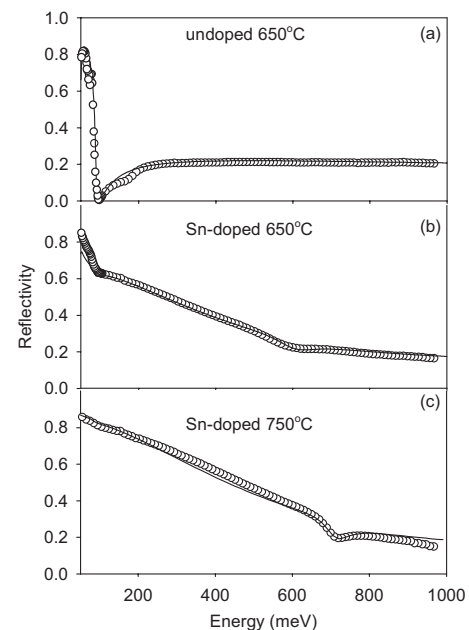


FIG. 5. Experimental infrared reflectance spectra (open circles) and spectra simulated using simple model dielectric function (solid lines). (a) Undoped In₂O₃ sample grown at 650 °C. (b) Sn-doped In₂O₃ sample grown at 650 °C. (c) Sn-doped In₂O₃ sample grown at 750 °C.

TABLE III. Plasma energies ($\hbar\omega_p$) and conduction electron scattering times (τ) resulting from simulation of IR reflectivity spectra. The derived values of plasmon damping energies (\hbar/τ) and carrier concentrations (n) are also given. The final column lists the positions of the Fermi level above the conduction band minimum (E_F) obtained from $\mathbf{k}\cdot\mathbf{p}$ calculations using the experimental value of n .

Sample	$\hbar\omega_p$ (meV)	τ (s)	\hbar/τ (meV)	n (cm ⁻³)	E_F (meV)
Undoped 650 °C	85	1.32×10^{-14}	50	7.5×10^{18}	21
Sn-doped 650 °C	600	5.98×10^{-15}	110	4.0×10^{20}	524
Sn-doped 750 °C	705	1.20×10^{-14}	55	5.6×10^{20}	648

contributions to the frequency dependent dielectric function $\varepsilon(\omega)$ of the epilayer, which was written in the form

$$\varepsilon(\omega) = \varepsilon(\infty) + \frac{[\varepsilon(0) - \varepsilon(\infty)]\omega_T^2}{\omega_T^2 - \omega^2 - i\omega\gamma} - \frac{\varepsilon(\infty)\omega_p^2}{\omega^2 + i\omega/\tau},$$

where $\varepsilon(0)$ and $\varepsilon(\infty)$ are the low and high frequency dielectric constants, ω_T is an effective transverse optical phonon frequency, and ω_p is the free carrier plasmon frequency. γ is the phonon damping constant and τ is the free carrier scattering time. The plasma frequency ω_p is itself given by

$$\omega_p^2 = \frac{ne^2}{\langle m^* \rangle \varepsilon(\infty) \varepsilon_0},$$

where n is the free carrier density, $\langle m^* \rangle$ is the density-of-states averaged electron effective mass and ε_0 is the permittivity of free space.

A transfer-matrix method was used to model transmission through the In₂O₃ epilayer and reflections at the air/In₂O₃ and In₂O₃/substrate interfaces, as well as incoherent reflections in the substrate. The key parameters to emerge from these analyses of the IR reflectivity data are given in Table III. The measured plasmon energies were used to derive values of carrier concentrations assuming an effective mass of $0.35m_0$ (where m_0 is the electron rest mass) and dielectric constants $\varepsilon(0)=8.9$ and $\varepsilon(\infty)=4.0$.⁴³ The carrier concentrations derived in this way are in generally good agreement with the Hall measurements. Moreover the free carrier scattering time for the film grown at 750 °C is roughly twice that for the sample grown at 650 °C, in agreement with the higher mobility for the latter. The scattering time for the nominally undoped film is, however, very similar to that for the Sn-doped sample grown at 750 °C and does not therefore mirror the reduced mobility in the undoped sample. We speculate that this discrepancy arises from the fact that the transport (Hall) measurements are more strongly influenced by grain boundary scattering than the plasmon broadening.

An alternative estimate of the free carrier plasma frequencies may be obtained from analysis of In $3d$ core level spectra in XPS shown in Fig. 6. The In core lines of the Sn doped samples show distinctly asymmetric profiles with development of a distinct low binding energy shoulder for the most highly doped sample. The spectra may be fitted with two Voigt components. The high binding energy component is the broader of the two and has a dominantly Lorentzian contribution to the line shape. Similar core level spectra have been found for related degenerately doped oxide systems in-

cluding PbO_{2-x},⁴⁴⁻⁴⁶ Ti₂O_{3-x},⁴⁷ and Sn_{1-x}Sb_xO₂.^{48,49} Two alternative approaches have been used to describe these complex line shapes. In a model developed by Kotani and Toyazawa⁵⁰ and Chalzalviel *et al.*,⁵¹ the low binding energy component corresponds to a final state where the core hole is

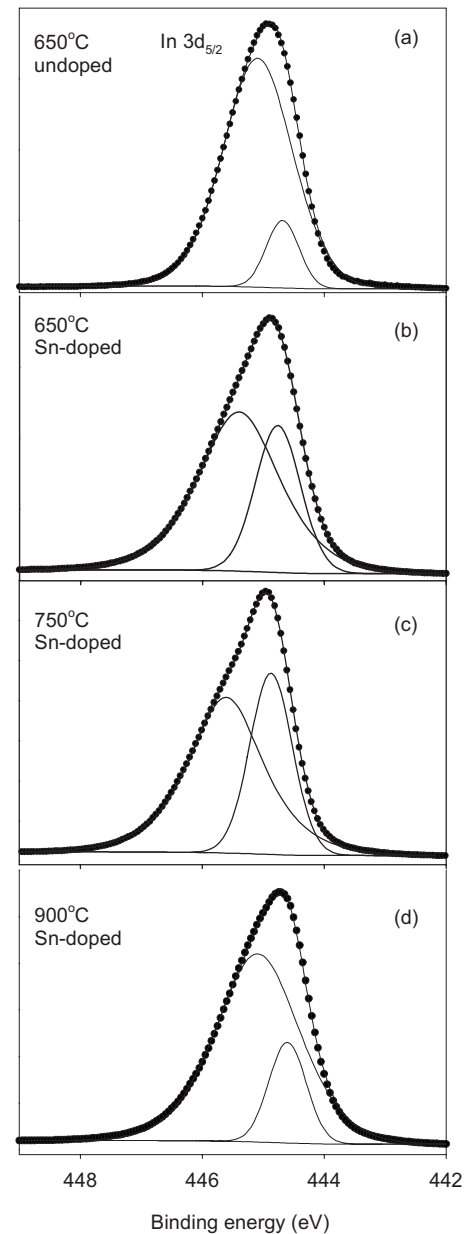


FIG. 6. Curve fits to the In $3d_{5/2}$ core line for (a) undoped In₂O₃ grown at 650 °C, (b) Sn-doped In₂O₃ grown at 650 °C, and (c) Sn-doped In₂O₃ grown at 750 °C.

TABLE IV. Binding energies (BEs), FWHMs, relative areas, and plasmon energies ($\hbar\omega_p$) derived from curve fits to In $3d_{5/2}$ spectral profiles.

Sample		BE (eV)	FWHM (eV)	Area	$\hbar\omega_p$ (meV)
Undoped 650 °C	Screened	444.69	0.63	0.12	410 ± 100
	Unscreened	445.10	1.34	0.88	
	Baricenter	444.95			
Sn-doped 650 °C	Screened	444.76	0.87	0.32	640 ± 50
	Unscreened	445.40	1.57	0.68	
	Baricenter	445.20			
Sn-doped 750 °C	Screened	444.86	0.82	0.38	740 ± 50
	Unscreened	445.61	1.44	0.62	
	Baricenter	445.32			
Sn-doped 900 °C	Screened	444.60	0.72	0.19	490 ± 100
	Unscreened	445.09	1.62	0.81	
	Baricenter	445.00			

screened by localization of a mobile conduction electron while the high binding energy component corresponds to a lifetime broadened unscreened final state. Alternatively the high binding energy component can be described as an unusually strong plasmon satellite.^{43,51,52} Previous work has shown that satellite energies in core XPS are close to plasmon loss energies measured in electron energy loss spectroscopy for both $\text{Sn}_{1-x}\text{Sb}_x\text{O}_2$ (Ref. 49) and PbO_{2-x} (Ref. 44).

The parameters derived from curve fits to the In $3d_{5/2}$ core lines are shown in Table IV. The separation between the two components of the core line is seen to be close to (but about 40 meV to greater than) the plasmon energies measured by IR reflectivity for the two Sn doped samples that were studied by infrared spectroscopy: the increase in plasmon energy between the samples grown at 650 and 750 °C is reproduced in the core XPS data. Moreover the relative intensity of the plasmon satellite *increases* as the carrier concentration *decreases*, as expected for the weak coupling model of excitation of plasmons by core holes in metallic systems.⁵¹ For the doped sample grown at 900 °C it was impossible to fit the IR reflectance data with a simple two-oscillator model. This is probably due to the incipient breakup of the film into islands, giving pronounced roughness on a length scale comparable with the wavelength of IR radiation. The films therefore had a milky appearance. In addition it was more difficult to obtain a unique and robust fit to the core line spectra for this sample because the satellite energy is comparable to the experimental resolution. However we can make a rough estimate of the carrier concentration by fitting the asymmetric In $3d$ core line profile with two components, as for the other doped samples. The best estimate of the XPS satellite energy of about 0.49 eV corresponds to a carrier concentration of $2.7 \times 10^{20} \text{ cm}^{-3}$. This is qualitatively in agreement with the intensity of the conduction band feature in valence XPS (see below). The core line for the nominally undoped sample grown at 650 °C also exhibits noticeable asymmetry. However, the two component curve fit to the core line for this sample using two components is the least robust of all the samples studied because the satellite energy is close to the experimental resolution. The best estimate numerical value of about 400 meV for the

satellite energy must therefore be treated with considerable caution, but suggests an effective surface carrier concentration of $1.9 \times 10^{20} \text{ cm}^{-3}$. This is clearly very much bigger than the measured bulk carrier concentration. There is thus at least qualitative evidence for surface electron accumulation over a length range comparable with the effective probing depth of Al $K\alpha$ XPS. This depth range can be quantified by noting that 95% of the XPS intensity derives from the region within 3λ of the surface, where λ is the electron inelastic mean free path. Assuming a “universal curve” value for λ of around 15 Å (Ref. 53), the effective probing depth at 45° take off angle is therefore about 30 Å.

We turn finally to a discussion of valence and conduction band spectra shown in Fig. 7. The onset at the Fermi energy contains a weak but well defined feature associated with occupied conduction band states and this can be used to provide a reference for the binding energy scale. The spectrum of the nominally undoped In_2O_3 is dominated by the O $2p$ valence band which has an onset energy as defined by linear extrapolation of the valence band edge at $2.95 \pm 0.05 \text{ eV}$ (Fig. 8). Sn doping leads to the appearance of new structure at the bottom of the valence band associated with states of mixed Sn $5s/\text{O } 2p$ character. However, the most striking effect of Sn doping is that the intensity of the conduction band feature is very strongly enhanced, particularly for the film grown at 750 °C. At the same time the valence band onset shifts to the higher energy of 3.20 eV for the 750 °C sample. These observations are consistent with upward movement of the Fermi level with increased filling of the conduction band as the carrier concentration increases. We have calculated the position of the Fermi level as a function of carrier concentration within the conduction band using a two band $\mathbf{k} \cdot \mathbf{p}$ model⁵⁴ which takes proper account of the pronounced non-parabolicity in the conduction band of In_2O_3 . The results of these calculations given in Table III are in excellent agreement with recent *ab initio* density functional calculation on Sn doped In_2O_3 based on large supercells.⁵⁵ The shift in the position of the valence band onset in XPS between the least and most highly doped samples (0.25 eV) is less than the calculated shift of 0.63 eV in the position of the Fermi energy. The discrepancy is due, in part, to bandgap renormal-

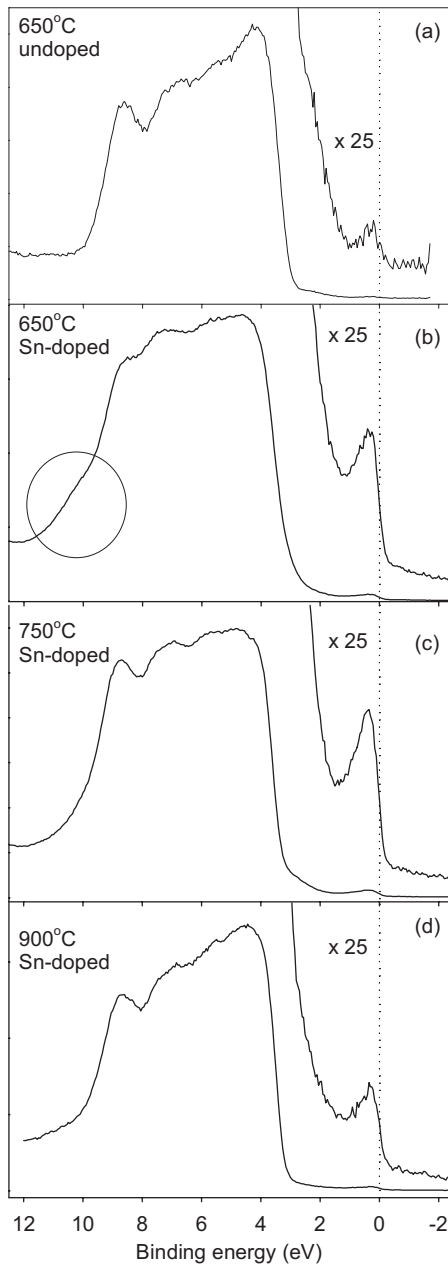


FIG. 7. Valence and conduction band XPS of (a) undoped In_2O_3 grown at 650 °C, (b) Sn-doped In_2O_3 grown at 650 °C, (c) Sn-doped In_2O_3 grown at 750 °C, (d) Sn-doped In_2O_3 grown at 900 °C. The circle in panel (b) highlights a feature at the bottom of the valence band associated with Sn 5s states.

ization or shrinkage with doping which arises mainly from stabilization of the lower conduction band states due to the enhanced attractive potential of Sn as compared with In. However the lowering of the shift due to bandgap renormalization is only about 0.15 eV (Ref. 55) and is not therefore big enough to account fully for the discrepancy between 0.63 and 0.25 eV. In addition the intensity of the conduction band feature in the spectrum of the nominally undoped sample is much too high relative to that of the most highly doped sample when considered in relation to the ratio of bulk carrier concentrations $7.5 \times 10^{18}/5.6 \times 10^{20} \sim 0.013$: clearly the conduction band feature for the nominally undoped sample is not ~ 75 times weaker than for the most highly doped

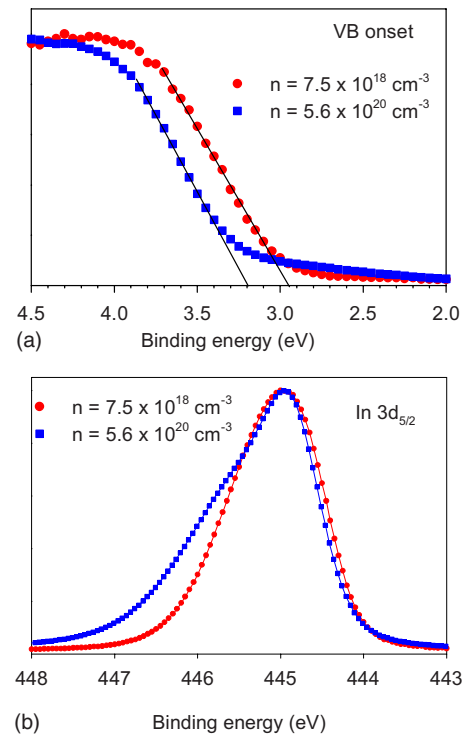


FIG. 8. (Color online) A comparison of (a) shifts in valence band onsets and (b) In $3d_{5/2}$ core level spectra for undoped samples grown at 650 °C ($n = 7.5 \times 10^{18} \text{ cm}^{-3}$) and Sn-doped sample grown at 750 °C ($n = 5.6 \times 10^{20} \text{ cm}^{-3}$). Note that the energy range for (b) is twice that for (a).

sample. As discussed in detail elsewhere, the valence and conduction band photoemission data for the nominally undoped samples are consistent with downward band bending at the surface by about 0.4 eV, with consequent electron accumulation to give carrier densities as high as $7 \times 10^{19} \text{ cm}^{-3}$ in a space charge region extending over around 50 Å.⁵⁶

IV. CONCLUDING REMARKS

We have shown that Sn doping in In_2O_3 has a very strong influence of the morphology of films grown by molecular beam epitaxy on Y-ZrO₂(100) substrates. In particular, incorporation of Sn into the films acts to inhibit the tendency of the In_2O_3 to break up into an array of square islands during high temperature growth. These changes may be traced to the fact that Sn doping leads to a small increase in the lattice parameter of the bcc bixbyite phase and better lattice matching with the substrate. At the same time optimal Sn doping during growth at 750 °C also leads to a twofold increase in carrier mobility, despite that fact the doping must introduce impurity scattering centers. Free electrons associated with Sn doping lead to pronounced changes in the infrared reflectivity of the films due to the presence of a conduction electron plasma. For the samples with a high Sn doping level the plasmon energy derived from analysis of the infrared data is found to lie at approximately the same energy as satellites in core level photoemission associated with final state screening effects.

ACKNOWLEDGMENTS

We are grateful to D.S.-L. Law and G. Beamson for technical assistance in XPS measurements. This work was supported by the EPSRC, U.K., under Grant Nos. EP/E031595/1 (Warwick), GR/S94148 (Oxford), and EP/E025722/1 (XPS facility).

- ¹M. Marezio, *Acta Crystallogr.* **20**, 723 (1966).
- ²Note, however, that the mechanism by which oxygen vacancies introduce charge carriers is still a matter of debate. See, for example, S. Lany and A. Zunger, *Phys. Rev. Lett.* **98**, 045501 (2007).
- ³I. Hamberg and C. G. Granqvist, *J. Appl. Phys.* **60**, 2950 (1986).
- ⁴C. G. Granqvist and A. Hultaker, *Thin Solid Films* **411**, 1 (2002).
- ⁵C. G. Granqvist, *Sol. Energy Mater. Sol. Cells* **91**, 1529 (2007).
- ⁶H. Hosono, *Thin Solid Films* **515**, 6000 (2007).
- ⁷G. Frank, H. Köstlin and A. Rabenau, *Phys. Status Solidi A* **52**, 231 (1979).
- ⁸N. Nanaud, N. Lequeux, M. Nanot, J. Jové, and T. Roisnel, *J. Phys. Chem. Solids* **135**, 140 (1998).
- ⁹H. Köstlin, R. Joost and W. Jems, *Phys. Stat. Solidi A* **29**, 87 (1975).
- ¹⁰G. Frank and H. Köstlin, *Appl. Phys. A* **27**, 197 (1982).
- ¹¹G. B. González, J. B. Cohen, J.-H. Hwang, T. O. Mason, J. P. Hodges, and J. D. Jorgensen, *J. Appl. Phys.* **89**, 2550 (2001).
- ¹²O. Warschkow, D. E. Ellis, G. B. González, and T. O. Mason, *J. Am. Ceram. Soc.* **86**, 1700 (2003).
- ¹³O. Warschkow, D. E. Ellis, G. B. González, and T. O. Mason, *J. Am. Ceram. Soc.* **86**, 1707 (2003).
- ¹⁴R. D. Shannon and C. T. Prewitt, *Acta Crystallogr., Sect. B: Struct. Crystallogr. Cryst. Chem.* **25**, 925 (1969).
- ¹⁵J. Popović, E. Tkalčec, B. Gržeta, C. Goebbert, V. Ksenofontov, and M. Takeda, *Z. Kristallogr.* **2007**, 489 (2007).
- ¹⁶M. Y. Chern, Y. C. Hunag, and X. L. Lu, *Thin Solid Films* **515**, 7866 (2007).
- ¹⁷H. Ohta, M. Orita, M. Hirano, H. Tanji, H. Kawazoe, and H. Hosono, *Appl. Phys. Lett.* **76**, 2740 (2000).
- ¹⁸H. Ohta, M. Orita, M. Hirano, and H. Hosono, *J. Appl. Phys.* **91**, 3547 (2002).
- ¹⁹T. Koida and M. Kondo, *J. Appl. Phys.* **99**, 123703 (2006).
- ²⁰Ch. Y. Wang, V. Lebedev, V. Cimalla, Th. Kups, K. Tonisch, and O. Ambacher, *Appl. Phys. Lett.* **90**, 221902 (2007).
- ²¹N. Taga, M. Maekawa, Y. Shigesato, I. Yasui, M. Kakei, and T. E. Haynes, *Jpn. J. Appl. Phys., Part 1* **37**, 6524 (1998).
- ²²Z. X. Mei, Y. Wang, X. L. Du, Z. Q. Zeng, M. J. Ying, H. Zheng, J. F. Jia, Q. K. Xue, and Z. Zhang, *J. Cryst. Growth* **289**, 686 (2006).
- ²³E. H. Morales, Y. He, U. Diebold, and B. Delley, *New J. Phys.* **10**, 125030 (2008).
- ²⁴M. Morinaga and J. B. Cohen, *Acta Crystallogr., Sect. A: Cryst. Phys., Diffraction, Theor. Gen. Crystallogr.* **35**, 789 (1979).
- ²⁵H. Horiuchi, A. J. Scultz, P. C. Leung, and J. M. Williams, *Acta Crystallogr., Sect. B: Struct. Sci.* **40**, 367 (1984).
- ²⁶In most crystallographic databases, material with 18% Y doping or less is reported to be tetragonal. The lattice parameter for cubic material with 17% Y doping is obtained by extrapolation from values of a for 28.0% doped material and 21.4% doped material.
- ²⁷A. Bourlange, D. J. Payne, R. G. Egdell, J. S. Foord, P. P. Edwards, M. O. Jones, A. Schertel, P. J. Dobson, and J. L. Hutchison, *Appl. Phys. Lett.* **92**, 092117 (2008).
- ²⁸A. Bourlange, D. J. Payne, R. M. J. Jacobs, R. G. Egdell, J. S. Foord, A. Schertel, P. J. Dobson, and J. L. Hutchison, *Chem. Mater.* **20**, 4551 (2008).
- ²⁹A. Bourlange, D. J. Payne, R. G. Palgrave, J. S. Foord, R. G. Egdell, R. M. J. Jacobs, A. Schertel, J. L. Hutchison, and P. J. Dobson, *Thin Solid Films* **517**, 4286 (2009).
- ³⁰A. Walsh, J. L. F. DaSilva, S.-H. Wei, C. Körber, A. Klein, L. F. J. Piper, A. DeMasi, K. E. Smith, G. Panaccione, P. Torelli, D. J. Payne, A. Bourlange, and R. G. Egdell, *Phys. Rev. Lett.* **100**, 167402 (2008).
- ³¹I. Hamberg, C. G. Granqvist, K.-F. Berggren, B. E. Sernelius, and L. Engström, *Phys. Rev. B* **30**, 3240 (1984).
- ³²A. Klein, *Appl. Phys. Lett.* **77**, 2009 (2000).
- ³³H. Raebiger, S. Lany, and A. Zunger, *Phys. Rev. Lett.* **101**, 027203 (2008).
- ³⁴P. D. C. King, T. D. Veal, D. J. Payne, A. Bourlange, R. G. Egdell, and C. F. McConville, *Phys. Rev. Lett.* **101**, 116808 (2008).
- ³⁵*Practical Surface Analysis*, 2nd ed., edited by D. Briggs and M. Seah (Wiley, Chichester, 1990).
- ³⁶R. G. Palgrave, A. Bourlange, D. J. Payne, and R. G. Egdell, *Cryst. Growth Des.* **9**, 1793 (2009).
- ³⁷M. Y. Tsai, M. E. White, and J. S. Speck, *J. Cryst. Growth* **310**, 4256 (2008).
- ³⁸B. Thiel and R. Helbig, *J. Cryst. Growth* **32**, 259 (1976).
- ³⁹M. Birkholz, *Thin Film Analysis by X-Ray Scattering* (Wiley-VCH, Weinheim, 2006).
- ⁴⁰M. Higuchi, S. Uekusa, R. Nakano, and K. Yokogawa, *J. Appl. Phys.* **74**, 6710 (1993).
- ⁴¹D. H. Zhang and H. L. Ma, *Appl. Phys. A: Mater. Sci. Process.* **62**, 487 (1996).
- ⁴²P. H. Jefferson, S. A. Hatfield, T. D. Veal, P. D. C. King, C. F. McConville, J. Zúñiga-Perez, and V. Munoz-Sanjosé, *Appl. Phys. Lett.* **92**, 022101 (2008).
- ⁴³V. Christou, M. Etschells, O. Renault, P. J. Dobson, O. V. Salata, G. Beamson, and R. G. Egdell, *J. Appl. Phys.* **88**, 5180 (2000).
- ⁴⁴D. J. Payne, R. G. Egdell, W. Hao, J. S. Foord, A. Walsh, and G. W. Watson, *Chem. Phys. Lett.* **411**, 181 (2005).
- ⁴⁵D. J. Payne, R. G. Egdell, D. S. L. Law, P. A. Glans, T. Learmonth, K. E. Smith, J. H. Guo, A. Walsh, and G. W. Watson, *J. Mater. Chem.* **17**, 267 (2007).
- ⁴⁶D. J. Payne, G. Paolicelli, F. Offi, G. Panaccione, P. Lacovig, G. Beamson, A. Fondacaro, G. Monaco, G. Vanko, and R. G. Egdell, *J. Electron Spectrosc. Relat. Phenom.* **169**, 26 (2009).
- ⁴⁷P. A. Glans, T. Learmonth, K. E. Smith, J. Guo, A. Walsh, G. W. Watson, F. Terzi, and R. G. Egdell, *Phys. Rev. B* **71**, 235109 (2005).
- ⁴⁸R. G. Egdell, J. Rebane, T. J. Walker, and D. S. L. Law, *Phys. Rev. B* **59**, 1792 (1999).
- ⁴⁹R. G. Egdell, T. J. Walker, and G. Beamson, *J. Electron Spectrosc. Relat. Phenom.* **128**, 59 (2003).
- ⁵⁰A. Kotani and Y. Toyazawa, *J. Phys. Soc. Jpn.* **37**, 912 (1974).
- ⁵¹J. N. Chazalviel, M. Campagna, and G. K. Wertheim, *Phys. Rev. B* **16**, 697 (1977).
- ⁵²D. J. Payne, J. P. Hu, R. G. Egdell, V. R. Dhanak, and G. Miller, *Chem. Phys. Lett.* **443**, 61 (2007).
- ⁵³G. A. Somorjai, *Chemistry in Two Dimensions: Surfaces* (Cornell University Press, Ithaca, 1981).
- ⁵⁴E. O. Kane, *J. Phys. Chem. Solids* **1**, 249 (1957).
- ⁵⁵A. Walsh, J. L. F. DaSilva, and S.-H. Wei, *Phys. Rev. B* **78**, 075211 (2008).
- ⁵⁶P. D. C. King, T. D. Veal, F. Fuchs, Ch. Y. Wang, D. J. Payne, A. Bourlange, H. Zhang, G. R. Bell, V. Cimalla, O. Ambacher, R. G. Egdell, F. Bechstedt, and C. F. McConville, *Phys. Rev. B* **79**, 205211 (2009).